

Modeling a Phased Array of Parametric Array Loudspeakers Using the Spherical Wave Expansion

Tao Zhuang[✉], Graduate Student Member, IEEE, Jia-Xin Zhong[✉], Member, IEEE, Guilin Ma, Feng Niu, and Jing Lu[✉], Member, IEEE

Abstract—Parametric array loudspeakers (PALs) that utilize the phased array technique are receiving considerable attention because of their ability to electronically control and manipulate highly directional audio beams with great flexibility. However, accurately modeling the phased array PAL poses significant challenges due to the complex nature of the nonlinear processes involved, which results in the demodulated audio sound generated by the array not simply being a superposition of that generated by each individual array element. In addition, the nonlinear interaction between the ultrasound generated by any two distinct elements creates a coupled audio sound component that also contributes to the total audio sound field. Based on the quasilinear solution of the Westervelt equation as well as the spherical wave expansion method, this paper proposed a computationally efficient and accurate method to include the coupled audio sound component. Both simulations and experiments for a uniform linear PAL array are conducted to validate the method. The proposed method paved the way for simulating and designing phased array PAL systems.

Index Terms—Directional audio beam, parametric array loudspeaker, parametric source, simulated annealing, spherical wave expansion, steerable beam.

I. INTRODUCTION

PARAMETRIC array loudspeakers (PALs) generate highly directional audio beams using an ultrasonic carrier wave in air [1], [2]. When a PAL radiates two harmonic A phased array PAL consisted with multiple PALs has been widely used in sound field control, such as beam steering, focusing and active noise control [3], [4], [5], [6], [7], [8]. In comparison to conventional loudspeaker arrays, PAL arrays offer the advantage of manipulating the audio sound field with minimal impact

Received 15 April 2024; revised 1 October 2024; accepted 16 December 2024. Date of publication 7 January 2025; date of current version 9 January 2025. The work of Tao Zhuang and Jing Lu was supported by National Natural Science Foundation of China under Grant 12274221. This work was supported by the AI & AI for Science Project of Nanjing University. The associate editor coordinating the review of this article and approving it for publication was Prof. Nobutaka Ito. (*Corresponding author: Jia-Xin Zhong.*)

Tao Zhuang and Jing Lu are with the Key Laboratory of Modern Acoustics, Nanjing University, Nanjing 210008, China, and also with the NJU-Horizon Intelligent Audio Lab, Horizon Robotics, Beijing 100094, China (e-mail: taozhuang@smail.nju.edu.cn; lujing@nju.edu.cn).

Jia-Xin Zhong is with the Graduate Program in Acoustics, Pennsylvania State University, University Park, PA 16802 USA (e-mail: jiaxin.zhong@psu.edu).

Guilin Ma is with Audfly Technology Suzhou Company Ltd., Suzhou 215163, China (e-mail: magl@audfly.com).

Feng Niu is with the Division of Mechanics and Acoustics, National Institute of Metrology, Beijing 100029, China (e-mail: niufeng@nim.ac.cn).

The implementation codes are available on: <https://github.com/TaoZhuang99/MCPAL-SWE>.

Digital Object Identifier 10.1109/TASLPRO.2024.3522764

outside of the target region [9]. This is primarily due to the high directivity of the audio sound generated by PALs [9], [10], [11]. However, the accurate and computationally efficient modeling of a phased array PAL remains a challenging task, which is the primary focus of this work.

The sound field generated by a PAL array can be categorized into three distinct regions: the near field, Westervelt far field, and inverse-law far field [12]. Recent studies have focused on accurately modeling the audio sound generated by a phased array PAL in the inverse-law far field, such as the convolution directivity model [3], [4], [13], [14]. However, the audio sound in the near field and the Westervelt far field is more intricate compared to the inverse-law far field, presenting a challenge for modeling these audio fields [12]. In the Westervelt far field, the acoustic waves generated by a PAL can be accurately modeled using the Westervelt equation. Since the ultrasound level produced by a PAL is generally restricted within a safety range [11], a quasilinear approximation can be assumed to simplify the Westervelt equation [15]. In the near field, the local nonlinear effects become dominant, necessitating an algebraic correction to the solution obtained from the Westervelt equation [16].

Under the framework of the quasilinear solution of the Westervelt equation, the calculation of the audio sound field necessitates numerical evaluations of five-fold integrals, which we refer to as the *direct integration method (DIM)* in this study [2]. Gaussian beam expansion methods have been proposed to simplify the calculation but it is inaccurate even in the paraxial region especially at low audio frequencies, because the main lobe of the virtual sources spreads outside the paraxial region [17], [18], [19], [20]. To solve this, a method known as the spherical wave expansion (SWE) was proposed [12], [15]. By representing the Green's function as a superposition of spherical harmonics, the computation can be simplified by leveraging azimuthal symmetry. Moreover, an improved SWE method using Zernike polynomials can model a steerable PAL without azimuthal symmetry [21]. However, it is important to note that the SWE method using Zernike polynomials becomes computationally expensive when the surface of the PAL array deviates from a circular shape, which causes difficulty in applying this method to a general phased array PAL consisting of circular emitters (elements) in practical applications.

The audio sound generated by a conventional electrodynamic loudspeaker array is typically expressed as the linear superposition of the sounds generated by individual loudspeakers [22], [23]. However, modeling a phased array PAL consisting of

circular elements presents two challenges. Firstly, the circular element of the phased array PAL cannot be modeled as a point source, as the ultrasound wavelength is typically comparable to, or smaller than, the size of the circular element. Secondly, the audio sound is generated due to the nonlinear interaction between two ultrasound waves with different frequencies. As a result, the audio sound generated by the phased array PAL is not only a sum of the audio sounds generated by each element individually but also includes the audio sounds resulting from the nonlinear interaction between two ultrasound waves with different frequencies from any two distinct elements. The audio sound caused by the interaction between any two different circular elements is referred to as “the coupled audio sound” in this work. To the best of the authors’ knowledge, existing literature on multi-channel PALs typically overlooks these coupled audio components, treating each array element individually [5], [24]. This may partly explain the discrepancies often observed between theoretical predictions and experimental measurements. This work underscores the importance of considering the coupled components.

The SWE method has been widely used for analyzing the performance of conventional loudspeaker arrays in various fields such as sound field reproduction and spatial audio [25], [26], [27], [28]. However, it has not been applied to phased array PALs due to the challenges in modeling the nonlinear process. This paper extends the SWE method with the additional theorem for spherical wave functions [29] to model the audio sound generated by a PAL array consisting of circular elements. First, the ultrasound generated by each individual element is computed in a local coordinate system. This local coordinate system is established based on each element, enabling the simplification of the Rayleigh integral through the application of the SWE method. Second, an additional theorem is employed to transform the ultrasound generated by each element from the local coordinate system to the global coordinate system [29]. This transformation allows the calculation of the total ultrasound generated by the PAL array by summing the ultrasounds generated by each individual element in the global coordinate system. Finally, utilizing the SWE method, the audio sound generated by the PAL array can be calculated in the global coordinate system. The proposed method is generally applicable to PAL arrays consisting of circular elements, which are common in practical applications. It is also found that when the distance between two transducers is sufficiently large, the coupling of their radiated audio sound becomes weak and negligible. As a result, the order of summation for total audio sound generated by the PAL array can be reduced for our proposed method, thereby decreasing the computational resources. To demonstrate its effectiveness, numerical results and experimental data are provided for a representative uniform linear PAL array. The efficacy of the proposed method is validated through comparisons with predictions obtained using the DIM.

II. THEORY

A. Problem Formulation

As shown in Fig. 1, N circular PAL array elements (ultrasonic transducers) are assumed to be located in the plane Oxy . The

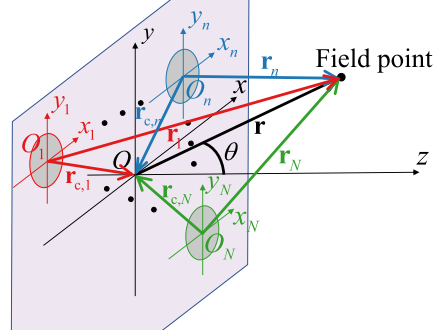


Fig. 1. The sketch of a PAL array consisting N circular elements. Various time delays can be applied to individual elements to achieve a phased array PAL.

n -th local coordinate system $O_n x_n y_n z_n$ are established with the origin O_n at the center of the n -th PAL, and the z_n -axis is perpendicular to the radiation surface of the PAL, where $n \in \{1, 2, \dots, N\}$. A global coordinate system $Oxyz$ is constructed for reference, where the xOy plane coincides with the $x_n O_n y_n$ plane and the positive x -axis, y -axis and z -axis parallel with the positive x_n -axis, y_n -axis and z_n -axis, respectively. The origin, O , of the global coordinate system is located at $\mathbf{r}_{c,n}$ under the n -th local coordinate system $O_n x_n y_n z_n$. For simplicity, the radius of all PAL elements is assumed to be identical of a . Each element generates two harmonic ultrasound waves at frequencies f_1 and f_2 ($f_1 < f_2$) with the same uniform amplitude of the vibration velocity v_0 on the surface. Hereafter, the subscript $u = 1$ and 2 represents the index of the ultrasound at frequencies f_1 and f_2 , respectively. The angular frequency of the ultrasound is expressed as $\omega_u = 2\pi f_u$.

Consider the ultrasound pressure at a point \mathbf{r}_v under the global coordinate system. For convenience, the coordinate of this point under the n -th local coordinate system is denoted by $\mathbf{r}_{v,n}$. They are related by $\mathbf{r}_v = \mathbf{r}_{v,n} - \mathbf{r}_{c,n}$. The ultrasound pressure at frequency f_u generated by the n -th PAL at $\mathbf{r}_{v,n}$ is denoted by $p_{u,n}(\mathbf{r}_{v,n}, \omega_u)$ in the n -th local coordinate system, which can be obtained using the Rayleigh integral in this local coordinate system to give

$$p_u(\mathbf{r}_v, \omega_u) = \sum_{n=1}^N p_{u,n}(\mathbf{r}_{v,n}, \omega_u), \quad (1)$$

where the time harmonic component $\exp(-i\omega_u t)$ is omitted for simplicity.

The audio sound is radiated by virtual audio sources with the source density of [12]

$$q(\mathbf{r}_v, \omega_a) = -\frac{i\beta\omega_a}{\rho_0^2 c_0^4} \sum_{i,j=1}^N p_{1,i}^*(\mathbf{r}_{v,i}, \omega_1) p_{2,j}(\mathbf{r}_{v,j}, \omega_2), \quad (2)$$

where i is the imaginary unit, β is the nonlinearity coefficient, the superscript “*” denotes the complex conjugate, ρ_0 is the air density, c_0 is the sound velocity in air, $\omega_a = 2\pi f_a$, and $f_a = f_2 - f_1$ is the audio frequency. Equation (2) indicates that q comprises two components: the virtual source density produced solely by the n -th element (where $i = j = n$), and the coupled component (where $i \neq j$) resulting from the nonlinear

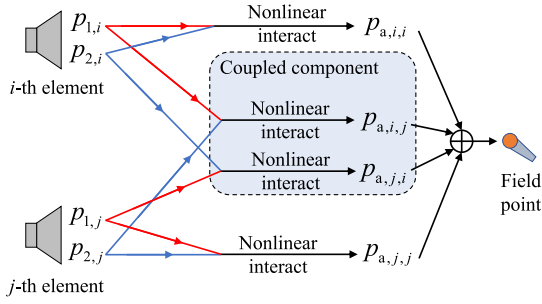


Fig. 2. The sketch of the audio sound generated by the i -th and the j -th elements of the PAL array. Red and blue lines denote the ultrasound at frequencies f_1 and f_2 , respectively.

interaction of the i -th and j -th elements. The audio sound at a field point \mathbf{r} under the global coordinate system can be obtained by substituting (2) into

$$p_a(\mathbf{r}, \omega_a) = -i\rho_0\omega_a \iiint_{-\infty}^{\infty} \frac{q(\mathbf{r}_v, \omega_a)}{4\pi|\mathbf{r} - \mathbf{r}_v|} e^{ik_a|\mathbf{r} - \mathbf{r}_v|} d^3\mathbf{r}_v, \quad (3)$$

where $k_a = \omega_a/c_0$ is the wavenumber of the audio sound [15]. In this work, we refer to the technique of computing audio sound by directly integrating (3) as the DIM. It is clear that because the DIM requires computing a five-fold integral after substituting the Rayleigh integral, it demands a significant amount of computational resources.

By substituting (2) into (3) and exchanging the order of summation and integration, the audio sound generated by the PAL array can be expressed as

$$p_a(\mathbf{r}, \omega_a) = \sum_{i,j=1}^N p_{a,i,j}(\mathbf{r}, \omega_a), \quad (4)$$

where $p_{a,i,j}$ represents the audio sound pressure generated by the nonlinear interaction of ultrasound wave at frequency f_1 radiated by the i -th element and the ultrasound wave at frequency f_2 radiated by the j -th element. It is expressed as

$$p_{a,i,j}(\mathbf{r}, \omega_a) = \frac{-\beta\omega_a^2}{4\pi\rho_0c_0^4} \times \iiint_{-\infty}^{\infty} \frac{p_{1,i}^*(\mathbf{r}_v, \omega_1)p_{2,j}(\mathbf{r}_v, \omega_2)}{|\mathbf{r} - \mathbf{r}_v|} e^{ik_a|\mathbf{r} - \mathbf{r}_v|} d^3\mathbf{r}_v. \quad (5)$$

For a special case when $i = j = n$, $p_{a,n,n}(\mathbf{r}, \omega_a)$ represents the audio sound solely generated by the n -th element. However, when $i \neq j$, $p_{a,i,j}(\mathbf{r}, \omega_a)$ represents the *coupled audio sound pressure*, as illustrated in Fig. 2. This coupled component, arising from system nonlinearity, highlights a significant distinction from conventional electrodynamic loudspeaker arrays.

B. SWE of the Ultrasound Field

According to the conventional SWE method, the ultrasound pressure generated by the n -th PAL in the local coordinate system $O_n x_n y_n z_n$ can be expressed as [15]

$$p_{u,n}(\mathbf{r}_v, \omega_u) = 4\pi p_0 \exp(i\omega_u \Delta t_n) \times \sum_{l=0}^{\infty} \mathcal{R}_{u,2l}(r_{v,n}) Y_{2l}^0(\theta_{v,n}, \varphi_{v,n}), \quad (6)$$

where Δt_n is the time delay of the n -th element, $p_0 = \rho_0 c_0 v_0$ is the on-surface pressure, $Y_{2l}^0(\theta_{v,n}, \varphi_{v,n})$ is the spherical harmonic function [30], and $r_{v,n}$, $\theta_{v,n}$ and $\varphi_{v,n}$ are the radial, zenithal, and azimuthal coordinates of $\mathbf{r}_{v,n}$ in the n -th local spherical coordinate system. The z_n -axis is denoted by $\theta_{v,n} = 0$. The time delay of the n -th PAL element at different ultrasonic frequencies is set to the same (Chap. 3.2 in [24]). The radial component for ultrasound can be obtained as [31]

$$\mathcal{R}_{u,2l}(r_{v,n}) = Y_{2l}^0(\pi/2, 0) h_{2l}(k_u r_{v,n}) \int_0^{k_u a} j_{2l}(\xi) \xi d\xi, \quad (7)$$

where k_u is the wavenumber of the ultrasound, $j_{2l}(\cdot)$ is the spherical Bessel function and $h_{2l}(\cdot)$ is the spherical Hankel function. Although (7) is inaccurate in the interior region $r_{v,n} < a$, it is usually negligible in practical applications. Equation (6) is expressed in the n -th local coordinate system and can be transformed into the global coordinate system using the spherical additional theorem [26], [29], [32],

$$p_{u,n}(\mathbf{r}_v, \omega_u) = \sum_{\nu_n=0}^{\infty} \sum_{\mu_n=-\nu_n}^{\nu_n} T_{\nu_n}^{\mu_n}(k_u \mathbf{r}_{c,n}) p_{\nu_n}^{\mu_n}(k_u \mathbf{r}_v, \omega_u), \quad (8)$$

where $p_{\nu_n}^{\mu_n}(k_u \mathbf{r}_v, \omega_u)$ is the ultrasound pressure of the mode (μ_n, ν_n) which is expressed as

$$p_{\nu_n}^{\mu_n}(k_u \mathbf{r}_v, \omega_u) = 4\pi p_0 \exp(i\omega_u \Delta t_n) \times \mathcal{R}_{\nu_n}(k_u r_v) Y_{\nu_n}^{\mu_n}(\theta_v, \varphi_v), \quad (9)$$

and the transformed coefficient $T_{\nu_n}^{\mu_n}$ of the mode (μ_n, ν_n) is obtained as

$$T_{\nu_n}^{\mu_n}(k_u \mathbf{r}_{c,n}) = \sum_{l=0}^{\infty} S_{2l,\nu_n}^{0,\mu_n}(k_u \mathbf{r}_{c,n}) \times Y_{2l}^0(\pi/2, 0) \int_0^{k_u a} j_{2l}(\xi) \xi d\xi. \quad (10)$$

The radial function in (9) can be expressed as

$$\mathcal{R}_{\nu_n}(x) = \begin{cases} j_{\nu_n}(x), & r_v \leq r_{c,n} \\ h_{\nu_n}(x), & r_v > r_{c,n} \end{cases}. \quad (11)$$

The additional coefficient in (10) is

$$S_{2l,\nu_n}^{0,\mu_n}(k_u \mathbf{r}_{c,n}) = 4\pi i^{\nu_n-2l} \sum_{\tau=|2l-\nu_n|}^{2l+\nu_n} i^\tau \mathcal{G}(2l, 0; \nu_n, -\mu_n; \tau) \times \hat{\mathcal{R}}_{\nu_n}(k_u r_{c,n}) Y_{\tau}^{\mu_n}(\theta_{c,n}, -\varphi_{c,n}), \quad (12)$$

where the hatted radial function is expressed as

$$\hat{\mathcal{R}}_{\nu_n}(x) = \begin{cases} h_{\nu_n}(x), & r_v \leq r_{c,n} \\ j_{\nu_n}(x), & r_v > r_{c,n} \end{cases}, \quad (13)$$

and the Gaunt coefficient is expressed as [29]

$$\begin{aligned} G(n, m; \nu, \mu; q) &= (-1)^{m+\mu} \sqrt{(2n+1)(2\nu+1)(2q+1)/4\pi} \\ &\times \begin{pmatrix} n & \nu & q \\ 0 & 0 & 0 \end{pmatrix} \begin{pmatrix} n & \nu & q \\ m & \mu & -m-\mu \end{pmatrix}. \end{aligned} \quad (14)$$

Here, $\begin{pmatrix} j_1 & j_2 & j \\ m_1 & m_2 & m \end{pmatrix}$ is the Wigner 3j symbol [12].

For a special case when O_n coincides with O ($r_{c,n} = 0$), the additional coefficient can be expressed as (Chap. 3.11 in [29])

$$S_{2l,\nu}^{0,\mu_n}(\mathbf{0}) = \delta_{2l,\nu} \delta_{0,\mu_n}, \quad (15)$$

where $\delta_{x,y}$ is the Kronecker delta function which vanishes unless $x = y$. By substituting (15), (10) and (9) into (8), the ultrasound pressure obtained using the additional theorem in (8) reduces to that obtained using the SWE method in (6).

C. SWE of the Coupled Audio Sound Field

Equations (8) and (9) show that the ultrasound pressure can be represented in the global coordinate system using separated spherical coordinates r_v , θ_v , and φ_v . Therefore, the coupled audio sound $p_{a,i,j}(\mathbf{r}, \omega_a)$ shown in (4) can also be obtained in the same manner by substituting (8) into (3). By using the SWE of the free field Green's function, the audio sound given by (3) can be expressed in the global spherical coordinate system as [21],

$$\begin{aligned} p_{a,i,j}(\mathbf{r}, \omega_a) &= \rho_0 c_0 k_a^2 \sum_{l_a=0}^{\infty} \sum_{m_a=-l_a}^{l_a} Y_{l_a}^{m_a}(\theta, \varphi) \\ &\times \int_0^{2\pi} \int_0^\pi \int_0^\infty q_{i,j}(\mathbf{r}_v, \omega_a) Y_{l_a}^{m_a,*}(\theta_v, \varphi_v) \\ &\times j_{l_a}(k_a r_{v,<}) h_{l_a}(k_a r_{v,>}) r_v^2 \sin \theta_v d\theta_v d\varphi_v, \end{aligned} \quad (16)$$

where $r_{v,<} = \min(r, r_v)$ and $r_{v,>} = \max(r, r_v)$. The coupled source density contributed by the ultrasound generated by the i -th element at f_1 and the j -th element at f_2 is obtained by substituting (8) into (2) to give

$$q_{i,j}(\mathbf{r}_v, \omega_a) = \sum_{\mathbf{v}, \boldsymbol{\mu}} q_{\mathbf{v}}^{\boldsymbol{\mu}}(\mathbf{r}_v, \omega_a), \quad (17)$$

where $\mathbf{v} = (\nu_i, \nu_j)$, $\boldsymbol{\mu} = (\mu_i, \mu_j)$ and the virtual audio source at mode $(\mathbf{v}, \boldsymbol{\mu})$ can be expressed as

$$\begin{aligned} q_{\mathbf{v}}^{\boldsymbol{\mu}}(\mathbf{r}_v, \omega_a) &= \frac{16\pi^2 \beta \omega_a p_0^2 \exp[i(\omega_2 \Delta t_j - \omega_1 \Delta t_i)]}{i\rho_0^2 c_0^4} \\ &\times T_{\nu_i}^{\mu_i,*}(k_1 \mathbf{r}_{c,i}) T_{\nu_j}^{\mu_j}(k_2 \mathbf{r}_{c,j}) \\ &\times \mathcal{R}_{\nu_i}^*(k_1 r_v) \mathcal{R}_{\nu_j}(k_2 r_v) Y_{\nu_i}^{\mu_i,*}(\theta_v, \varphi_v) Y_{\nu_j}^{\mu_j}(\theta_v, \varphi_v) \end{aligned} \quad (18)$$

The substitution of (17) and (18) into (16) yields the audio sound pressure as

$$p_{a,i,j}(\mathbf{r}, \omega_a) = \sum_{\mathbf{v}, \boldsymbol{\mu}} p_{\mathbf{v}}^{\boldsymbol{\mu}}(\mathbf{r}, \omega_a), \quad (19)$$

where the audio sound pressure contributed by $q_{\mathbf{v}}^{\boldsymbol{\mu}}(\mathbf{r}_v, \omega_a)$ at mode $(\mathbf{v}, \boldsymbol{\mu})$ is expressed as

$$\begin{aligned} p_{\mathbf{v}}^{\boldsymbol{\mu}}(\mathbf{r}, \omega_a) &= \frac{16\pi^2 \beta p_0^2 \exp[i(\omega_2 \Delta t_j - \omega_1 \Delta t_i)]}{i\rho_0 c_0^2} \\ &\times \sum_{l_a=0}^{\infty} \sum_{m_a=-l_a}^{l_a} T_{\nu_i}^{\mu_i,*}(k_1 \mathbf{r}_{c,i}) T_{\nu_j}^{\mu_j}(k_2 \mathbf{r}_{c,j}) \end{aligned}$$

$$\begin{aligned} &\times Y_{l_a}^{m_a}(\theta, \varphi) \int_0^\infty j_{l_a}(k_a r_{v,<}) h_{l_a}(k_a r_{v,>}) \\ &\times \mathcal{R}_{\nu_i}^*(k_1 r_v) \mathcal{R}_{\nu_j}(k_2 r_v) k_a^3 r_v^2 dr_v \\ &\times Y_{l_a}^{m_a,*}(\theta_v, \varphi_v) \sin \theta_v d\theta_v d\varphi_v. \end{aligned} \quad (20)$$

According to the integration of triple spherical harmonics (Appendix B in [29]) expressed as

$$\begin{aligned} &\int_0^{2\pi} \int_0^\pi Y_{\nu_i}^{\mu_i,*}(\theta_v, \varphi_v) Y_{\nu_j}^{\mu_j}(\theta_v, \varphi_v) \\ &\times Y_{l_a}^{m_a,*}(\theta_v, \varphi_v) \sin \theta_v d\theta_v d\varphi_v \\ &= \delta_{\mu_i - \mu_j - m_a, 0} (-1)^{\mu_i} \mathcal{G}(\nu_i, -\mu_i; \nu_j, \mu_j; l_a). \end{aligned} \quad (21)$$

This integral makes use of the orthogonality properties of $\exp(im_a \varphi_v)$, as spherical harmonic function involves terms of the form $\exp(im_a \varphi_v)$. Then (20) is simplified to

$$\begin{aligned} p_{\mathbf{v}}^{\boldsymbol{\mu}}(\mathbf{r}, \omega_a) &= \frac{16\pi^2 \beta p_0^2 \exp[i(\omega_2 \Delta t_j - \omega_1 \Delta t_i)]}{i\rho_0 c_0^2} \\ &\times (-1)^{\mu_i} \sum_{l_a=|\mu_i - \mu_j|}^{\infty} \mathcal{G}(\nu_i, -\mu_i; \nu_j, \mu_j; l_a) \\ &\times \mathcal{R}_{\mathbf{v}, l_a}^{\boldsymbol{\mu}}(r) Y_{l_a}^{\mu_i - \mu_j}(\theta, \varphi), \end{aligned} \quad (22)$$

where the radial component for audio sound is obtained as

$$\begin{aligned} \mathcal{R}_{\mathbf{v}, l_a}^{\boldsymbol{\mu}}(r) &= T_{\nu_i}^{\mu_i,*}(k_1 \mathbf{r}_{c,i}) T_{\nu_j}^{\mu_j}(k_2 \mathbf{r}_{c,j}) \\ &\times \int_0^\infty j_{l_a}(k_a r_{v,<}) h_{l_a}(k_a r_{v,>}) \\ &\times \mathcal{R}_{\nu_i}^*(k_1 r_v) \mathcal{R}_{\nu_j}(k_2 r_v) k_a^3 r_v^2 dr_v. \end{aligned} \quad (23)$$

In summary, the audio sound pressure, $p_a(\mathbf{r}, \omega_a)$ in (4), is decomposed into different contributions, denoted as $p_{a,i,j}(\mathbf{r}, \omega_a)$ representing the audio sound pressure generated by the non-linear interaction between the i -th and j -th elements. Each contribution, $p_{a,i,j}(\mathbf{r}, \omega_a)$, as shown by (19), is expressed as the summation of $p_{\mathbf{v}}^{\boldsymbol{\mu}}(\mathbf{r}, \omega_a)$, which represents the audio sound pressure contributed by the virtual source density after applying the addition theorem, $q_{\mathbf{v}}^{\boldsymbol{\mu}}(\mathbf{r}, \omega_a)$. Specifically, $p_{\mathbf{v}}^{\boldsymbol{\mu}}(\mathbf{r}, \omega_a)$ can be calculated using (22) with the radial component (23).

III. NUMERICAL RESULTS

The proposed method is applicable to an arbitrary phased array PAL consisting of circular elements. For simplicity, the commonly used uniform linear PAL array is chosen for numerical analysis. The uniform linear PAL array consists of N circular PAL elements with a radius of a . The center of all elements is located on the x -axis. Without loss of generality, the x_n -axis of each local coordinate system coincides with the global x -axis. The distance between adjacent PAL elements is uniform and denoted by Δx and the center of the uniform linear PAL array coincides with O .

TABLE I
PARAMETERS USED IN SIMULATIONS

Symbol	Definition	Value
T	Ambient temperature	20°C
h_r	Relative humidity of air	60%
a	Size of the PAL element	5 mm
f_u	Center frequency of the ultrasound	40 kHz
α_u	Attenuation coefficients of the ultrasound	0.15 Np/m
v_0	Amplitude of the velocity profile	0.1 m/s
β	Nonlinear coefficient	1.2

Table I lists the parameters used in the simulations, where the center frequency of the ultrasound is $f_u = (f_1 + f_2)/2$. For a conventional loudspeaker array, the total audio sound field is simply the superposition of the audio sound generated by each array element. Therefore, the summation of the audio sound generated by each PAL element (linear solution) is denoted by “Uncoupled solution” in this work. In contrast, the summation of both the uncoupled and coupled audio sound components obtained using the proposed method is denoted as the “Coupled solution”.

For comparison, the results obtained using the DIM are presented. The integration domain of Rayleigh integral is defined cover the surface of the PAL array, which is $-0.08 \text{ m} \leq x_s \leq 0.08 \text{ m}$ and $-0.03 \text{ m} \leq y_s \leq 0.03 \text{ m}$. The integration domain of volume integral (3) is set to cover the major portion of the ultrasonic beam, which is $-0.8 \text{ m} \leq x_v \leq 0.8 \text{ m}$, $-0.8 \text{ m} \leq y_v \leq 0.8 \text{ m}$, and $-3 \text{ m} \leq z_v \leq 3 \text{ m}$. All integration domains are discretized with a resolution of half the ultrasound wavelength (approximately 4.3 mm). The three-point Gaussian-Legendre quadrature is then applied to evaluate the numerical integration within each discretized range.

A. Sound Fields Generated by Two PAL Elements

This section investigates the simplest configuration of a phased array PAL system, comprising only two ($N = 2$) ultrasonic transducers (elements). Furthermore, a time delay of 0 is applied to both elements. The centers of the two elements are both located on the x -axis and are symmetric relative to the y -axis, meaning that $x_{c,1} = -x_{c,2}$, $y_{c,1} = y_{c,2} = 0$, $z_{c,1} = z_{c,2} = 0$. The convergence and accuracy of the proposed method will be examined and compared to the Rayleigh integral.

1) *Convergence Analysis*: Fig. 3 depicts the calculation error of ultrasound pressure, which is defined as the difference between the sound pressure level (SPL) obtained using the proposed method and Rayleigh integral, at typical field points for two different separations between the two PAL elements of (a) 10 mm and (b) 30 mm, with respect to the truncated term ν in (8). It is clear that all the curves converge as the truncated term increases. Specifically, the ΔSPL is less than 0.1 dB when the truncated term is $\nu = 8$ and $\nu = 25$ when the separation is 10 mm and 30 mm, respectively. In the subsequent simulations, the results with $\nu = 40$ are presented for the ultrasound.

Fig. 4 illustrates the calculation error of audio sound pressure, which is defined as the difference between the SPL obtained using the proposed method and the DIM, at several typical field

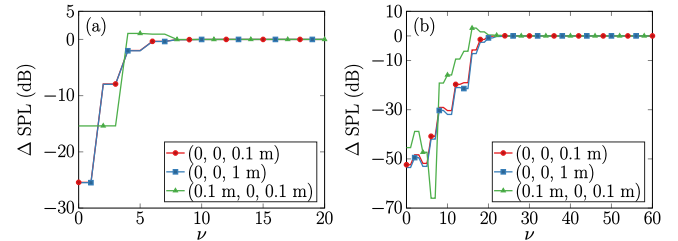


Fig. 3. The ultrasound pressure error generated by two circular PAL elements, obtained using the proposed method with different truncation terms of $\nu = \nu_1 = \nu_2$ in (8), is shown for element separations of (a) 10 mm and (b) 30 mm. The curves with circle, square, and triangle markers represent the ultrasound pressure at field points $(0, 0, 0.1 \text{ m})$, $(0, 0, 1 \text{ m})$, and $(0.1, 0, 0.1 \text{ m})$, respectively.

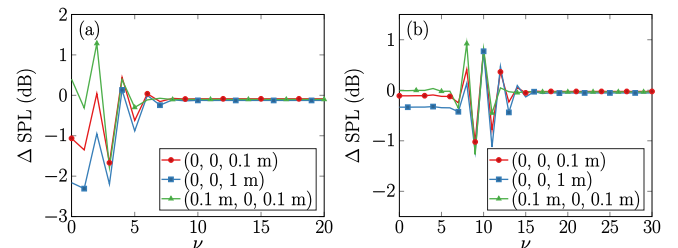


Fig. 4. The audio sound pressure error generated by two circular PAL elements, obtained using the proposed method with different truncation terms of ν in (19), is shown for element separations of (a) 10 mm and (b) 30 mm. The curves with circle, square, and triangle markers represent the audio sound pressure at field points $(0, 0, 0.1 \text{ m})$, $(0, 0, 1 \text{ m})$, and $(0.1, 0, 0.1 \text{ m})$, respectively.

points for two different separations between the two circular PAL elements of (a) 10 mm and (b) 30 mm, with respect to the truncated term ν in (19). It can be observed that all the curves converge as the truncated term increases. For example, the ΔSPL is less than 0.1 dB when the truncated term is $\nu = 8$ and $\nu = 15$ for the separations of 10 mm and 30 mm, respectively. Therefore, the truncated term ν for the audio sound is set as 20 in the subsequent simulations. It can be observed that when the interval between the elements is 30 mm, the convergence order of the audio sound ($\nu = 15$) is lower than that of the ultrasound ($\nu = 25$). This is because the spatial resolution required for the source density function is determined by the audio sound wavelength (see (3)). Since the audio sound wavelength is greater than that of the ultrasound, the audio sound field can still be accurately calculated even if the spatial resolution of the ultrasonic field is slightly lower.

2) *Ultrasound Field*: Fig. 5 shows the axial ultrasound on the z -axis and the angular ultrasound 1 m away from point O on the Oxz plane, calculated using the proposed method and Rayleigh integral. It can be observed that the ultrasound obtained using the proposed method is consistent with the exact solution obtained using Rayleigh integral. It is also noted that there are some lobes in the ultrasound due to the interference phenomenon, as the separation of two PAL elements is larger than the ultrasound wavelength [33]. The results of the Fig. 5 validate the accuracy of the ultrasound obtained using the proposed method.

3) *Audio Sound Field*: Fig. 6 illustrates the axial and angular audio sound generated by two PAL elements with different

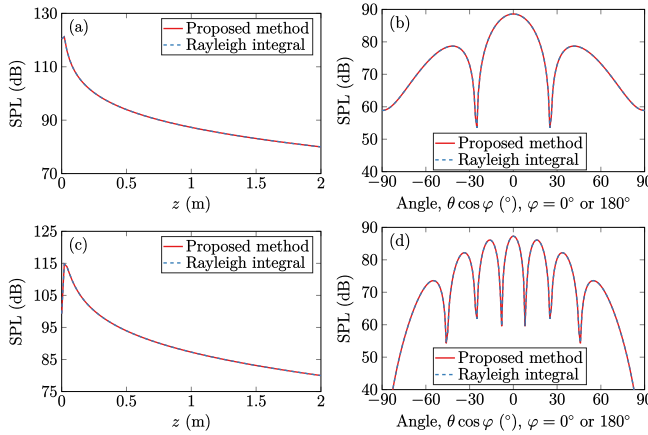


Fig. 5. The ultrasound pressure generated by two circular PAL elements at 40 kHz, obtained using the proposed method (solid lines) and Rayleigh integral (dashed lines), is shown for element separations of (top row) 10 mm and (bottom row) 30 mm. Left column: axial SPL; right column: angular SPL located at 1 m away from point O on the Oxz plane.

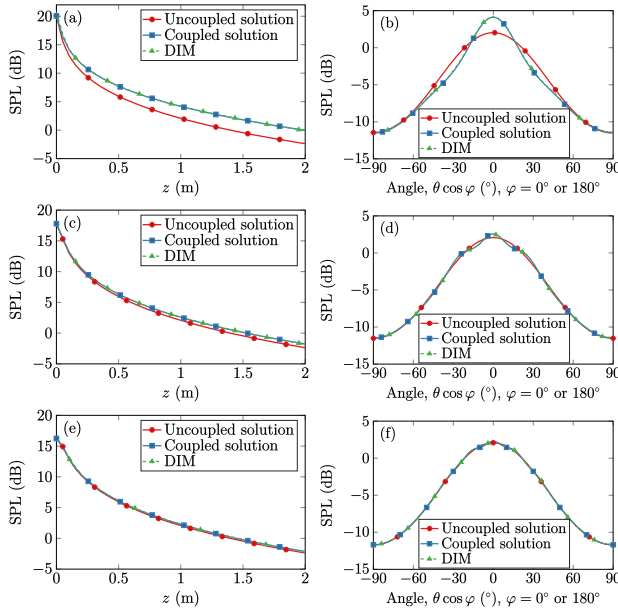


Fig. 6. The audio sound pressure generated by two circular PAL elements at 1 kHz. Left column: axial audio SPL; right column: angular audio SPL located at 1 m away from O on the Oxz plane. The separation between the two circular PAL elements is (top) 10 mm, (middle) 20 mm and (bottom) 30 mm. The curves with circle, square, and triangle marks represent the uncoupled solution, the coupled solution and the DIM, respectively.

separations. It is evident that the uncoupled solution has significant errors, while the coupled solution is consistent with the exact solution obtained using the DIM. For instance, when the separation between two PAL elements is 10 mm, the axial SPL error of the uncoupled solution is approximately 2.5 dB at a field point 2 m away from O , whereas the error of the coupled solution is less than 0.1 dB. Meanwhile, the angular SPL error between the coupled solution and exact solution is less than 0.1 dB at all angles. Moreover, it is observed that the angular audio sound of the coupled solution is sharper than that of the

uncoupled solution. As shown in Fig. 6(b), when the separation between the two PAL elements is 10 mm, the difference between the SPLs at 0° and 30° of the coupled solution is approximately 9 dB, while that of the uncoupled solution is only around 3 dB. The uncoupled solution is the summation of the audio sound generated by two PAL elements themselves with a separation Δx . Consequently, the audio beam of the uncoupled solution is broader than that generated by a single PAL element.

On the other hand, the virtual audio source density (2) generated due to the overlap of two ultrasound beams becomes narrower when the beams are offset by a certain distance. Consequently, the coupled audio sound generated by the virtual audio source density is narrower compared to the audio signal produced by a single transducer.

As the separation between two PAL elements increases, the uncoupled solution progressively converges towards the exact solution. For example, when the separation between two PAL elements is 10 mm, the axial SPL error of the uncoupled solution at the field point 2 m away from O is around 2.5 dB. However, when the separation between two PAL elements increases to 30 mm, both the axial and angular SPL errors of the uncoupled solution are less than 0.1 dB. The reason for this is that when the separation between two PAL elements increases, the cross-area of the main lobes of the ultrasound generated by both PALs decreases, resulting in a decrease in the density of the virtual audio source.

B. Sound Fields Generated by a Uniform Linear PAL Array

The uniform linear PAL array considered in this section consists of 10 circular PAL elements with a separation of 10 mm between adjacent elements. According to Section III-A, when the separation of two PAL elements is larger than 30 mm, the coupled audio component can be neglected without introducing significant errors. Therefore, in this section, the coupled audio sound needs to be considered only when the separation between any two PALs is 10 mm and 20 mm.

1) Uniform Linear PAL Array Without the Beam Steering: Fig. 7 presents the axial and angular audio sound generated by the uniform linear PAL array at 1 m away from O for different audio frequencies. In this case, beam steering is disabled, resulting in a time delay of 0 applied to all elements. Similar to the sound field generated by two PAL elements in Section III-A, the axial SPL of the coupled solution is larger than that of the uncoupled solution, and the difference between the coupled and the uncoupled solution increases as the audio frequency increases. For example, the difference in axial SPL generated by the uniform linear PAL array 2 m away from O between the coupled and uncoupled solutions is around 3 dB, 4.5 dB, and 5 dB for 500 Hz, 1 kHz, and 2 kHz, respectively. Additionally, the audio sound pressure at the main lobe (0°) increases with audio frequency, as it is approximately proportional to the square of the frequency, as shown in (4) and (5).

The comparison between the DIM and the coupled solution reveals that the DIM yields a higher audio sound level, which is primarily due to the contribution of the coupled audio sound between two PAL elements with a separation larger than 20 mm.

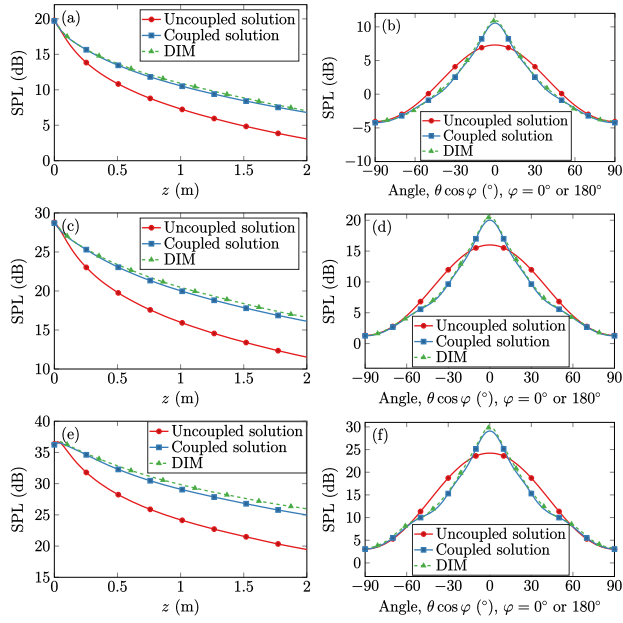


Fig. 7. The audio sound pressure generated by a uniform linear PAL array consisting of 10 circular elements with the element separation of $\Delta x = 10$ mm. The beam steering angle is 0° . Left column: axial audio SPL; right column: angular SPL located at 1 m away from O on the Oxz plane, the audio frequency is (top) 500 Hz, (middle) 1 kHz, and (bottom) 2 kHz. The curves with circle, square and triangle marks represent the uncoupled solution, the coupled solution and the exact solution, respectively.

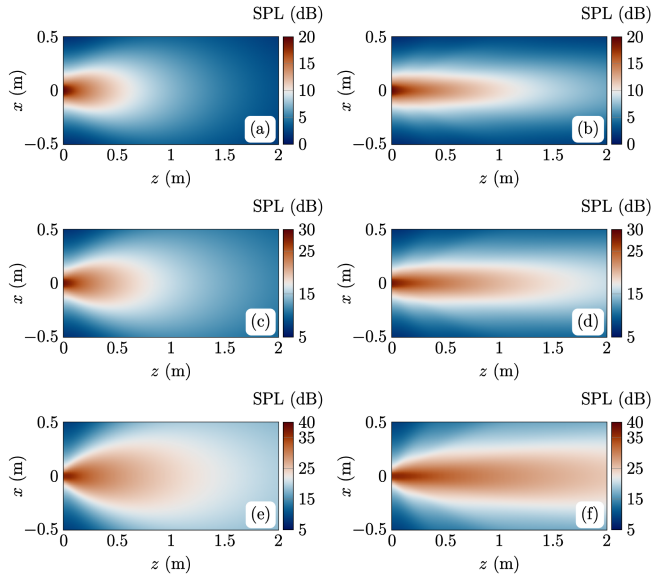


Fig. 8. The audio sound field generated by a uniform linear PAL array consisting of 10 circular elements with the element separation of $\Delta x = 10$ mm on the Oxz plane. The beam steering angle is 0° . Left column: the uncoupled solution; right column: the coupled solution, the audio frequency is (top) 500 Hz, (middle) 1 kHz, and (bottom) 2 kHz.

Nonetheless, this discrepancy is negligible and can be ignored for practical purposes. For example, the axial SPL error between the coupled solution and the DIM is less than 1 dB at 2 m and 2 kHz. Fig. 8 shows the audio sound field obtained using the uncoupled and coupled solutions. It can be observed that the

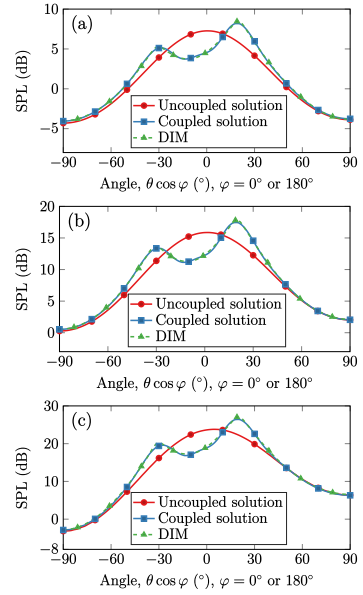


Fig. 9. The angular audio sound pressure generated by a phased array PAL consisting of 10 circular elements with the element separation of $\Delta x = 10$ mm 1m away from O on the Oxz plane. The audio frequency is (top) 500 Hz, (middle) 1 kHz, and (bottom) 2 kHz. The beam steering angle is 20° . The curves with circle, square and triangle marks represent the uncoupled solution, the coupled solution and the exact solution, respectively.

directivity of the coupled solution is higher than that of the uncoupled solution.

2) *Uniform Linear PAL Array With the Beam Steering:* The steering angle from the positive z -axis to the positive x -axis on the Oxz plane is denoted by $\theta_s \in (0, \pi/2)$, while the steering angle from the positive z -axis to the negative x -axis on the Oxz plane is denoted by $-\theta_s$. Then the time delay of the n -th PAL element can be expressed as $\Delta t_n = n\Delta x \sin \theta_s / c_0$.

Fig. 9 shows the angular audio SPL generated by the uniform linear PAL array with a steering angle $\theta_s = 20^\circ$ at 500 Hz, 1 kHz, and 2 kHz. The corresponding angle of the main lobe obtained using the coupled solution is consistent with the steering angle, but the angle obtained using the uncoupled solution is less than the steering angle. For instance, when the audio frequency is 2 kHz, the corresponding angle of the peak of the uncoupled solution is around 5° , while that of the main lobe of the coupled solution is around the steering angle 20° . Similar to the observation in Section III-B1, the directivity of the coupled solution is narrower than that of the uncoupled solution. In the case of beam steering, the broad directivity obtained using the uncoupled solution results in the main lobe and the second lobe of the audio beam being indistinguishable. After including the coupled audio sound components between array elements, the main and second lobes of the audio beam can be well distinguished. This is also presented in Fig. 10, which shows the two-dimensional (2D) audio sound field generated by this phased array PAL with the beam steering on the Oxz plane obtained using the uncoupled or coupled solutions. In the coupled solution, the main lobe and the second lobe of the audio beam are clearly observed. These simulation results demonstrate the importance of considering the coupled audio sound when modeling phased array PALs.

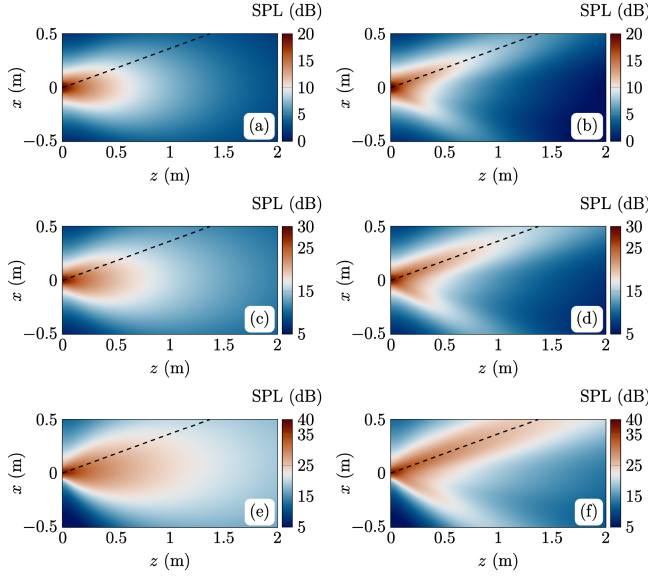


Fig. 10. The audio sound field generated by a phased array PAL consisting of 10 circular elements with the element separation of $\Delta x = 10$ mm on the Oxz plane. Left column: the uncoupled solution; right column: the coupled solution, the audio frequency is (top) 500 Hz, (middle) 1 kHz, and (bottom) 2 kHz. The beam steering angle is 20°. The dashed line represents the steering direction, the steering angle is 20°.

TABLE II
COMPUTATIONAL COST OF THE PROPOSED METHOD AND DIM

	Calculation time (s)	Memory (GB)
Proposed method (One point)	532.3	1.7
DIM (One point)	7253.2	99.7
Proposed method (2D field)	86889.1	1.7
DIM (2D field)	$7253.2 \times 100 \times 100$	99.7

Additionally, it is noted that the maximum value of the angular audio sound decreases when considering steering compared to the no-steering case. This reduction occurs because the element interval (10 mm) exceeds the ultrasonic wavelength (8.6 mm), resulting in the formation of side lobes. Consequently, the energy of the main lobe decreases, leading to a lower maximum value of the angular audio sound.

C. Computation Efficiency

Table II shows the calculation time and the required memory of the proposed method and DIM for an on-axis point ($x = 0, y = 0, z = 1$ m) and a 2D field points (100×100 points). The results are obtained on a computer with a 2.1 GHz CPU and 1 TB random access memory.

Although only one field point needs to be calculated, the computational time required for obtaining DIM given by (3) exceeds 7000 s. This excessive time consumption is primarily due to the numerical evaluation challenges associated with the five-fold integral. Additionally, the DIM demands a significant amount of memory (99.7 GB in Table II) because the source density at all three-dimensional (3D) virtual points is required to store. Consequently, the direct integration of (3) has generally not been adopted in literature. In contrast, the proposed method exhibits the potential to achieve a speed increase of over 13

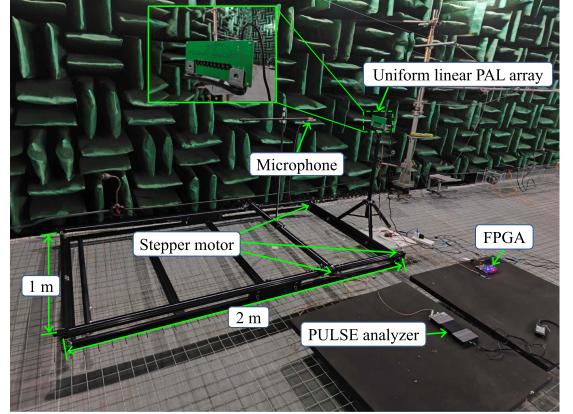


Fig. 11. A photo of the experiment setup.

times while requiring significantly less memory. This is achieved by reducing the integral to a one-fold operation and utilizing five-fold summations, as described in (22) and (23).

The advantages of the proposed method are more profound when calculating the 2D sound field distribution, illustrated by considering a grid of 100×100 field points. The proposed method involves pre-computation of the 2D coupled audio distribution between each pair of two transducers and its storage. Subsequently, the 2D total audio sound field generated by the PAL array is efficiently obtained by weighting and shifting the stored data. The memory required by the proposed method is independent of the number of field points to be calculated, remaining fixed at 1.7 GB. As shown in Table II, the calculation time of the proposed method increases to around 87000 s. Conversely, the calculation time required by the DIM increases linearly with the number of field points, leading to exceeding 7×10^7 s to compute the 2D field with a grid of 100 by 100 points. In conclusion, the proposed method requires only 1/58 of the memory but is over 800 times faster than the DIM. Through the simulation results, it becomes apparent that the proposed method can accurately predict the audio sound field, closely resembling DIM, while drastically reducing the computational cost.

IV. EXPERIMENTS

A. Experimental Setup

In order to verify the accuracy of the proposed method, a prototype of a uniform linear PAL array was fabricated, as depicted in Fig. 11. The prototype comprises ten circular ultrasonic emitters (Murata MA40S4S, Kyoto, Japan), each with a resonance frequency of 40 kHz and a radius of 5 mm. The ultrasonic emitters are arranged in a linear array with a spacing of 10 mm, and the time delay for each emitter can be controlled to realize a phased array PAL. The multi-channel independent rectangular pulse signals are generated by an FPGA (Xilinx XC7A100T, San Jose, CA) and power amplified by MOSFET drivers (Microchip MIC4127, Chandler, AZ) [6]. The logical diagram of the circuits is identical to Fig. 8 in [34]. The signal at each channel consists of two pulse signals at two ultrasonic frequencies: 39.744 kHz and 40.256 kHz (or 39.496 kHz and 40.52 kHz, or 39 kHz and

40.984 kHz), resulting in the generation of an audio sound wave at 512 Hz (or 1024 Hz, 1984 Hz). The FPGA operates at a clock rate of 50 MHz, enabling precise phase differences between channels through signal time shifting with a resolution of only 0.02 μ s. The beam steering angle is set to 20 degrees, and the time delay between the adjacent PAL elements in the uniform linear PAL array is around 10 μ s, which can be realized by programming the FPGA.

The experiments were conducted in an anechoic room at Nanjing University, which has dimensions of 11.4 m \times 7.8 m \times 6.7 m (height). The relative humidity and temperature were 27% and 26 °C, respectively. The photograph of the experimental setup is shown in Fig. 11. Sound pressure was measured using a condenser microphone Type CHZ-221 (Hangzhou Acoustic Sensing Technology Co., Ltd., Hangzhou, China). The signal is conditioned and analyzed by a PULSE analyzer (Brüel & Kjær Type 3160). To mitigate spurious sound induced by the intense ultrasonic waves, the microphone was covered with a thin piece of plastic film [6], and the insertion loss of the film has been compensated in the experimental results. The sound field in a rectangular area, with dimensions of 1 m \times 2 m and a step size of 40 mm, was measured as depicted in Fig. 11. The surface of the PAL elements is perpendicular to the measurement plane. The microphone was positioned at the same height as the center of the PAL and scanned by three stepper motors, which were controlled by personal computers. Although the physical radius of the ultrasonic emitter is 5 mm, preliminary measurements (not presented for conciseness) indicated that the effective radiation radius is only approximately 3.2 mm. Consequently, the simulation results in comparison to measured ones in this section were obtained by assuming circular ultrasonic emitters with a radius of 3.2 mm.

B. Measurement Results

The measurement results in the rectangular area and the corresponding simulation results at 512 Hz, 1024 Hz, and 1984 Hz, both without and with the beam steering at a steering angle of 20°, are depicted in Figs. 12 and 13, respectively.

The predictions generally align well with the measured sound field. It can be observed that for azimuth angles greater than 60°, the audio SPL of the simulation results is lower than that of the experimental results. This discrepancy can be attributed to the normalized directivity of the MA40S4S, which is less than -10 dB for azimuth angles exceeding 60° while the normalized directivity of the simulation is around -5 dB when the azimuth angle is 60°. Consequently, the practical virtual source density in these directions is lower than that of the simulation. Furthermore, the simulation assumes an infinite baffle for the PAL array, while in the experimental setup, the baffle used for the prototype is approximately only 20 cm in length and 8 cm in width. While this size is much larger than the ultrasound wavelength (8.6 mm at 40 kHz), it is smaller than the wavelength of audio sound (e.g., 34 cm at 1 kHz). This discrepancy in baffle size contributes to the differences between the simulation and experimental results [35].

Additionally, it is evident that at an audio frequency of 512 Hz, the audio beam shown in measurements appears sharper

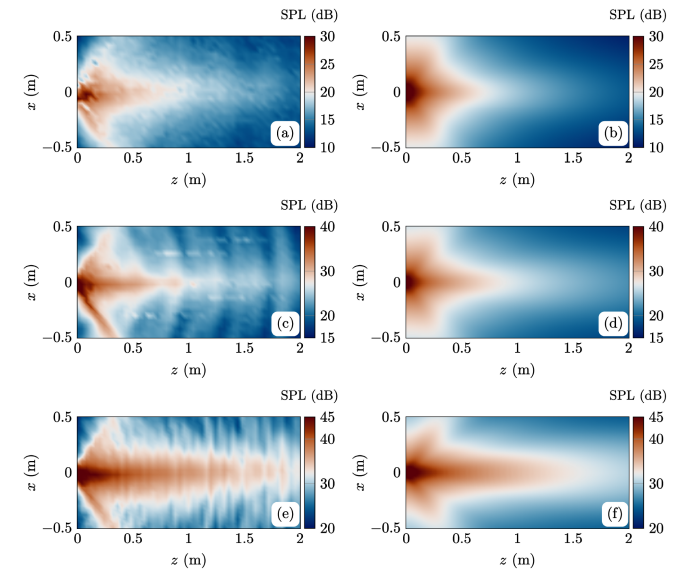


Fig. 12. Measured audio sound pressure field generated by the uniform linear PAL array consisting of 10 circular elements with the element separation of $\Delta x = 10$ mm on the Oxz plane. The beam steering angle is 0°. Left column: experiment results; right column: simulation results. The audio frequency is (top) 512 Hz, (middle) 1024 Hz, and (bottom) 1984 Hz.

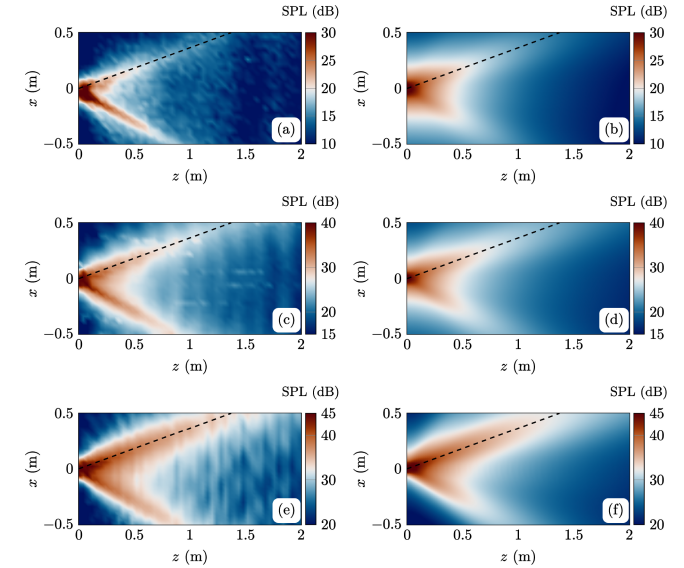


Fig. 13. Measured audio sound pressure field generated by the phased array PAL consisting of 10 circular elements with the element separation of $\Delta x = 10$ mm on the Oxz plane. Left column: experiment results; right column: simulation results. The audio frequency is (top) 512 Hz, (middle) 1024 Hz, and (bottom) 1984 Hz. The dashed line represents the steering direction, the steering angle is 20°.

compared to the simulation results. This disparity arises from the directivity characteristics of the MA40S4S, which exhibit attenuation at larger angles. In the near field, the sound pressure generated by an ultrasound emitter with a smaller azimuth angle is greater than that generated by another ultrasound emitter with a larger azimuth angle, which results in a narrower beam in the experiments than that in numerical simulations. However, as the

audio frequency increases, the audio beam becomes sharper, reducing the influence of the directivity of the practical ultrasonic emitter. Consequently, the simulation results align better with the experimental results as depicted in Figs. 12 and 13.

V. CONCLUSION

This work proposed a computationally efficient and accurate method for calculating the audio sound generated by a phased array PAL consisting of circular elements. The method involves solving the quasilinear solution of the Westervelt equation, which reveals that the audio sound produced by the PAL array can be expressed as a sum of the audio sounds generated by each element individually, as well as the coupled audio sounds generated by any two different elements. The audio sound generated by one element individually can be obtained using the existing SWE method [15], while the coupled audio sounds generated by any two different elements can be calculated by integrating the additional theorem of the spherical wave functions. The simulation results demonstrate the accuracy and the efficiency of the proposed method compared to the direct numerical integration of the quasilinear solution in audio sound calculation. Moreover, the experimental results provide further evidence of the accuracy and reliability of the proposed method. This method indicates that modeling the PAL array differs from conventional loudspeaker arrays. While the audio sound generated by a conventional loudspeaker array is the sum of sounds produced by each element individually, the PAL array's modeling requires considering not only the uncoupled solution but also the coupled audio sounds between any two different elements due to the nonlinearity of the PAL array. The proposed method has paved the way for simulating and designing phased array PAL systems, enabling the manipulation of highly directional audio beams with greater precision and control.

REFERENCES

- [1] P. J. Westervelt, "Parametric acoustic array," *J. Acoust. Soc. Amer.*, vol. 35, no. 4, pp. 535–537, 1963.
- [2] J. Zhong and X. Qiu, *Acoustic Waves Generated by Parametric Array Loudspeakers*. Boca Raton, FL, USA: CRC Press, 2024.
- [3] C. Shi, Y. Kajikawa, and W.-S. Gan, "An overview of directivity control methods of the parametric array loudspeaker," *APSIPA Trans. Signal Inf. Process.*, vol. 3, 2014, Art. no. e20.
- [4] W.-S. Gan, J. Yang, K.-S. Tan, and M.-H. Er, "A digital beamsteerer for difference frequency in a parametric array," *IEEE/Trans. Audio, Speech, Lang. Process.*, vol. 14, no. 3, pp. 1018–1025, May 2006.
- [5] Y. Ogami, M. Nakayama, and T. Nishiura, "Virtual sound source construction based on radiation direction control using multiple parametric array loudspeakers," *J. Acoust. Soc. Amer.*, vol. 146, no. 2, pp. 1314–1325, 2019.
- [6] J. Zhong et al., "Low frequency audio sound field generated by a focusing parametric array loudspeaker," *IEEE/ACM Trans. Audio, Speech, Lang. Process.*, vol. 30, pp. 3098–3109, 2022.
- [7] N. Tanaka and M. Tanaka, "Active noise control using a steerable parametric array loudspeaker," *J. Acoust. Soc. Amer.*, vol. 127, no. 6, pp. 3526–3537, 2010.
- [8] Y. Li and W. Zheng, "A noise control method using adaptive adjustable parametric array loudspeaker to eliminate environmental noise in real time," *Int. J. Environ. Res. Public Health*, vol. 19, no. 1, 2021, Art. no. 269.
- [9] J. Zhong, T. Zhuang, R. Kirby, M. Karimi, H. Zou, and X. Qiu, "Quiet zone generation in an acoustic free field using multiple parametric array loudspeakers," *J. Acoust. Soc. Amer.*, vol. 151, no. 2, pp. 1235–1245, 2022.
- [10] C. Shi and W.-S. Gan, "Product directivity models for parametric loudspeakers," *J. Acoust. Soc. Amer.*, vol. 131, no. 3, pp. 1938–1945, 2012.
- [11] W.-S. Gan, J. Yang, and T. Kamakura, "A review of parametric acoustic array in air," *Appl. Acoust.*, vol. 73, no. 12, pp. 1211–1219, 2012.
- [12] J. Zhong, R. Kirby, and X. Qiu, "The near field, westervelt far field, and inverse-law far field of the audio sound generated by parametric array loudspeakers," *J. Acoust. Soc. Amer.*, vol. 149, no. 3, pp. 1524–1535, 2021.
- [13] O. Guasch and P. Sánchez-Martín, "Far-field directivity of parametric loudspeaker arrays set on curved surfaces," *Appl. Math. Model.*, vol. 60, pp. 721–738, 2018.
- [14] J. Zhong, H. Zou, J. Lu, and D. Zhang, "A modified convolution model for calculating the far field directivity of a parametric array loudspeaker," *J. Acoust. Soc. Amer.*, vol. 153, no. 3, pp. 1439–1451, 2023.
- [15] J. Zhong, R. Kirby, and X. Qiu, "A spherical expansion for audio sounds generated by a circular parametric array loudspeaker," *J. Acoust. Soc. Amer.*, vol. 147, no. 5, pp. 3502–3510, 2020.
- [16] M. Červenka and M. Bednářík, "An algebraic correction for the Westervelt equation to account for the local nonlinear effects in parametric acoustic array," *J. Acoust. Soc. Amer.*, vol. 151, no. 6, pp. 4046–4052, 2022.
- [17] C. Ye, M. Wu, S. Wu, C. Huang, and J. Yang, "Modeling of parametric loudspeakers by Gaussian-beam expansion technique," *Jpn. J. Appl. Phys.*, vol. 49, no. 7S, 2010, Art. no. 07HE18.
- [18] M. Červenka and M. Bednářík, "Non-paraxial model for a parametric acoustic array," *J. Acoust. Soc. Amer.*, vol. 134, no. 2, pp. 933–938, 2013.
- [19] T. Zhuang, J. Zhong, F. Niu, M. Karimi, R. Kirby, and J. Lu, "A steerable non-paraxial Gaussian beam expansion for a steerable parametric array loudspeaker," *J. Acoust. Soc. Amer.*, vol. 153, no. 1, pp. 124–136, 2023.
- [20] Y. Zhu, W. Ma, Z. Kuang, M. Wu, and J. Yang, "Optimal audio beam pattern synthesis for an enhanced parametric array loudspeaker," *J. Acoust. Soc. Amer.*, vol. 154, no. 5, pp. 3210–3222, 2023.
- [21] J. Zhong, R. Kirby, M. Karimi, and H. Zou, "A spherical wave expansion for a steerable parametric array loudspeaker using zernike polynomials," *J. Acoust. Soc. Amer.*, vol. 152, no. 4, pp. 2296–2308, 2022.
- [22] J.-W. Choi and Y.-H. Kim, "Generation of an acoustically bright zone with an illuminated region using multiple sources," *J. Acoust. Soc. Amer.*, vol. 111, no. 4, pp. 1695–1700, 2002.
- [23] Z. Han, M. Wu, Q. Zhu, and J. Yang, "Three-dimensional wave-domain acoustic contrast control using a circular loudspeaker array," *J. Acoust. Soc. Amer.*, vol. 145, no. 6, pp. EL488–EL493, 2019.
- [24] C. Shi, "Investigation of the steerable parametric loudspeaker based on phased array techniques," Ph.D. dissertation, Nanyang Technol. Univ., Singapore, 2013.
- [25] D. B. Ward and T. D. Abhayapala, "Reproduction of a plane-wave sound field using an array of loudspeakers," *IEEE Trans. Audio, Speech, Lang. Process.*, vol. 9, no. 6, pp. 697–707, Sep. 2001.
- [26] Y. J. Wu and T. D. Abhayapala, "Theory and design of soundfield reproduction using continuous loudspeaker concept," *IEEE Trans. Audio, Speech, Lang. Process.*, vol. 17, no. 1, pp. 107–116, Jan. 2009.
- [27] Y. J. Wu and T. D. Abhayapala, "Spatial multizone soundfield reproduction: Theory and design," *IEEE Trans. Audio, Speech, Lang. Process.*, vol. 19, no. 6, pp. 1711–1720, Aug. 2011.
- [28] F. Winter, J. Ahrens, and S. Spors, "On analytic methods for 2.5-D local sound field synthesis using circular distributions of secondary sources," *IEEE/ACM Trans. Audio, Speech, Lang. Process.*, vol. 24, no. 5, pp. 914–926, May 2016.
- [29] P. A. Martin, *Multiple Scattering: Interaction of Time-Harmonic Waves With N. Obstacles*. Cambridge, U.K.: Cambridge Univ. Press, 2006.
- [30] B. Rafaely and A. Avni, "Interaural cross correlation in a sound field represented by spherical harmonics," *J. Acoust. Soc. Amer.*, vol. 127, no. 2, pp. 823–828, 2010.
- [31] K. G. Foote, "Discriminating between the nearfield and the farfield of acoustic transducers," *J. Acoust. Soc. Amer.*, vol. 136, no. 4, pp. 1511–1517, 2014.
- [32] H. Sun, T. D. Abhayapala, and P. N. Samarasinghe, "A realistic multiple circular array system for active noise control over 3D space," *IEEE/ACM Trans. Audio, Speech, Lang. Process.*, vol. 28, pp. 3041–3052, 2020.
- [33] L. W. Schmerr Jr., *Fundamentals of Ultrasonic Phased Arrays*. Berlin, Germany: Springer, 2014.
- [34] A. Marzo, T. Corkett, and B. W. Drinkwater, "Ultraino: An open phased-array system for narrowband airborne ultrasound transmission," *IEEE Trans. Ultrason., Ferroelectr. Freq. Control*, vol. 65, no. 1, pp. 102–111, Jan. 2018.
- [35] J. Zhong, R. Kirby, and X. Qiu, "A non-paraxial model for the audio sound behind a non-baffled parametric array loudspeaker," *J. Acoust. Soc. Amer.*, vol. 147, no. 3, pp. 1577–1580, 2020.